ONLINE MEASUREMENT METHOD FOR TRACTOR DRIVE WHEEL SLIP RATIO BASED ON IMA-PKF

/

基于 IMA-PKF 的拖拉机驱动轮滑转率在线测量方法研究

Shenghui FU[1,2)], Ruqi TANG [1)], Naixv REN[1)], Xinzhe ZHANG[1)], Ruixin LAN[1)], Wen ZHANG[*1,2)]
[1)] College of Mechanical and Electronic Engineering, Shandong Agricultural University, Taian 271018 / China;
[2)] Shandong Engineering Research Center of Agricultural Equipment Intelligentization, Taian 271018 / China
Tel: +8618811126258; E-mail: wenzhang098@ sdau.edu.cn; Corresponding author: Wen Zhang
DOI: https://doi.org/10.35633/inmateh-77-13

Keywords: *tractor; slip ratio estimation; improved Mayfly algorithm; parallel Kalman filtering algorithm*

ABSTRACT

Accurate and real-time measurement of tractor drive wheel slip ratio under plowing conditions is essential for improving overall machine performance and tillage quality. To address the limitations of existing methods—namely low measurement accuracy, poor anti-interference capability, and low efficiency—this study proposes an online slip ratio measurement method based on multi-sensor fusion and adaptive filtering. A real-time measurement system was developed by integrating GNSS, IMU, and wheel encoders. Furthermore, a lens-based quasi-oppositional learning strategy and a good-point-set initialization mechanism were introduced to enhance the mayfly algorithm, which was then used to optimize a parallel Kalman filter, forming the improved mayfly algorithm–parallel Kalman filter (IMA-PKF). This approach enables adaptive real-time adjustment to random noise disturbances encountered during plowing operations, thereby enhancing robustness. Simulation results show that under non-interference conditions, the IMA-PKF algorithm achieves a root mean squared error (RMSE) of 0.0214, representing a 74.8% reduction compared with the conventional KF algorithm. In addition, compared with PSO-PKF and MA-PKF, the RMSE accuracy is improved by approximately 62.23% and 49.41%, respectively. When disturbance points are introduced, IMA-PKF still maintains the lowest estimation error, with an RMSE of 0.0359, demonstrating excellent stability and anti-interference capability. Field experiments under different plowing depths further validate the robustness of the method: the maximum slip ratio measurement error is only 1.94%, with bias controlled within 2%. Compared with KF, the proposed method reduces mean absolute error (MAE) and RMSE by up to 36.29% and 37.06%, respectively. Overall, the IMA-PKF algorithm enables accurate and stable online measurement of tractor drive wheel slip ratio under diverse plowing conditions, providing a solid theoretical and technical foundation for improving tractor performance and operational efficiency.

摘要

犁耕工况下拖拉机驱动轮滑转率的在线准确测量对提升拖拉机作业性能和犁耕质量具有重要意义。为解决当前犁耕工况下拖拉机滑转率滑转率测量精度低、抗干扰能力差、测量效率低等问题，本文提出一种基于多传感器融合与自适应滤波的拖拉机滑转率在线测量方法。首先，本文利用 GNSS、IMU 与轮速编码器等多源传感器搭建了拖拉机滑转率在线测量系统。然后，引入基于透镜成像的准对立学习策略与优点集初始化机制，构建了基于改进蜉蝣算法优化的并行卡尔曼滤波算法（IMA-PKF），实现了犁耕作业随机噪声扰动的自适应实时调整，增强了算法对犁耕工况的鲁棒性。仿真结果表明，无干扰条件下，IMA-PKF 算法下滑转率的估计值 RMSE 为 0.0214，较传统 KF 降低 74.8%，优于 PSO-PKF 和 MA-PKF，分别提升 62.23%、49.41%；引入扰动点后， RMSE 仅为 0.0359，具有良好的稳定性与抗干扰能力。田间试验结果进一步验证了该方法在不同耕深工况下的鲁棒性，滑转率测量值最大误差仅 1.94%，偏差控制 2%以内，较 KF 算法下的 MAE 和 RMSE 分别降低 36.29%与 37.06%。综上，IMA-PKF 算法实现了不同犁耕工况下拖拉机驱动轮滑转率的在线准确测量，为提升拖拉机整机性能和作业效率奠定了理论基础和技术支撑。

INTRODUCTION

Slip ratio is a critical parameter for evaluating tractor traction performance and operational efficiency (*Pranav et al., 2012; Zhang et al., 2025*). Both excessively low and high slip ratio adversely affect traction, reducing efficiency and posing safety risks (*Du et al., 2024; Xia et al., 2021*). Therefore, accurately measuring the slip ratio is essential for improving the level of tractor performance and operational effectiveness *(Raheman & Jha, 2007*).

The accuracy of tractor slip ratio depends on precise measurement of theoretical and actual tractor speeds (*Shoutao Li et al., 2024*). However, complex field conditions introduce various noise interferences. Traditional methods, such as the fifth-wheel and minimum wheel speed methods, are susceptible to ground undulations and thus unsuitable for complex agricultural environments. Single encoder-based measurements suffer from white noise and unmeasurable disturbances (*Boisvert & Micheau, 2016*). GPS-based speed measurement can also fail under conditions such as canopy occlusion or cloud cover. Consequently, single-sensor systems cannot ensure high-accuracy real-time measurement under diverse conditions. Multi-sensor data fusion has emerged to enhance slip ratio estimation accuracy *(Cao et al., 2015; Han et al., 2023; Peng et al., 2025; Wang et al., 2021*). The key to such fusion lies in the design of an appropriate state estimation algorithm. Among existing techniques, the Kalman filter (KF) is widely used in vehicle state estimation due to its excellent dynamic estimation capability and noise suppression performance *(Bisht & Singh, 2014; Deng et al., 2024; Suzuki, 2013*). However, KF accuracy heavily depends on properly specified process and measurement noise covariance matrices. Sensor noise in agricultural environments often exhibits time-varying, delayed, and stochastic behaviors, complicating accurate modeling (*De Bruijn & Gill, 2014)*. Moreover, standard KF applies unified observation modeling across sensors, neglecting their distinct characteristics and reducing estimation accuracy. In contrast, the Parallel Kalman Filter (PKF) framework allows for constructing independent observers for each sensor, enabling separate filtering and fusion of estimation results. This not only improves estimation precision but also enhances system robustness. PKF has been widely applied in domains such as train state estimation (*Wen et al., 2023*), multi-target tracking, and autonomous navigation (*Liu et al., 2024; Xiong et al., 2020*), demonstrating strong robustness and adaptability. To further enhance the robustness of the Kalman filter in noisy and dynamic environments, various adaptive optimization methods have been proposed in recent years by researchers both domestically and internationally. For example, Sun improved the innovation-based adaptive Kalman filter by incorporating chi-square testing to dynamically adjust measurement noise covariance and reject abnormal measurements, enhancing the stability and accuracy of INS/GPS integration (*Sun et al., 2022*). Li developed a GA-LSTM-based framework that identifies the current road surface condition in real time and dynamically adjusts the noise covariance matrices of the KF accordingly (*Shaohua Li et al., 2024*). In another study, Li applied a particle swarm optimization (PSO) algorithm to adaptively tune the environmental noise parameters of the KF, thereby improving its prediction accuracy *(Li et al., 2022*). Although these methods have shown improvements in the adaptability of the KF to some extent, they still suffer from several limitations, such as complex parameter tuning processes, insufficient real-time performance, and limited robustness under highly variable environmental conditions.

Given the above, A slip ratio of tractor drive wheels online measurement based on Improved Mayfly Algorithm-Parallel Kalman Filter (IMA-PKF) was proposed in this paper. The method adaptively adjusts filter parameters via online estimation of noise covariance matrices and fuses multi-sensor data from tractor slid ratio online measurement system through a parallel Kalman filtering framework. And it is possible to achieve real-time, accurate and robust online measurement of the tractor slip ratio under complex plowing conditions.

MATERIALS AND METHODS

Tractor Slip Ratio Measurement System and Modeling

The system state model characterizes the dynamic behavior of the tractor slip ratio measurement system. In this study, the sideslip angle is not considered, and only longitudinal slip is taken into account. The system state includes the actual vehicle speed, the longitudinal acceleration of the vehicle body, and its rate of change, $\boldsymbol{x}(k)$ is defined as:

$$\boldsymbol{x}(k) = [v_e(k)\ a_e(k)\ a_e'(k)\ v_q(k)\ a_q(k)\ a_q'(k)]^{\mathrm{T}} \quad (1)$$

where: $v_e(k)$ denotes the actual vehicle speed at time step k, m/s, $a_e(k)$ is the vehicle body acceleration, m/s²; $a_e'(k)$ represents the rate of change of the acceleration, m/s³, $v_q(k)$ is the theoretical vehicle speed, m/s, $a_q(k)$ denotes the theoretical acceleration, m/s², and $a_q'(k)$ is the rate of change of the theoretical acceleration, m/s³. k is the discrete-time index, and the superscript T denotes the matrix transpose.

The linear system state transition equation is given by:

$$\boldsymbol{x}(k+1) = \boldsymbol{A}\cdot\boldsymbol{x}(k) + \boldsymbol{w}(k) \quad (2)$$

where $\boldsymbol{A}$ is the state transition matrix, defined as: $\boldsymbol{A}=\begin{bmatrix} 1 & \Delta t & 0.5\Delta t^2 & 0 & 0 & 0 \\ 0 & 1 & \Delta t & 0 & 0 & 0 \\ 0 & 0 & 1 & 0 & 0 & 0 \\ 0 & 0 & 0 & 1 & \Delta t & 0.5\Delta t^2 \\ 0 & 0 & 0 & 0 & 1 & \Delta t \\ 0 & 0 & 0 & 0 & 0 & 1 \end{bmatrix}$, where Δt is the sampling time interval, $\boldsymbol{w}(k)$ is zero-mean Gaussian white noise with a covariance matrix $\boldsymbol{Q}$, and denotes the uncertainty in the system.

To improve the estimation accuracy of the tractor drive wheel slip ratio, a Parallel Kalman Filter (PKF) structure is adopted, consisting of two independent observers, $\boldsymbol{Z}_1$ and $\boldsymbol{Z}_2$, which process measurements from Global Navigation Satellite System (GNSS), photoelectric encoders, and the Inertial Measurement Unit (IMU), respectively. The PKF approach enables separate local estimations at each observer node using its own sensor data, and these local estimates are subsequently fused to obtain a global state estimate *(Hashemipour et al., 1988*). The final optimal estimate is obtained through weighted fusion of the two observers. The observation vector $\boldsymbol{Z}_1$(k) and $\boldsymbol{Z}_2$(k) are defined as:

$$\begin{cases} \boldsymbol{Z}_1(k)=[v_{qe}(k)\ a_{qe}(k)\ 0\ v_{te}(k)\ a_{te}(k)\ 0]^{\mathrm{T}} \\ \boldsymbol{Z}_2(k)=[v_{qg}(k)\ a_{qe}(k)\ 0\ v_{te}(k)\ a_{te}(k)\ 0]^{\mathrm{T}} \end{cases} \quad (3)$$

where, $v_{qe}(k)$ denotes the actual vehicle speed measured by the encoder, m/s, $a_{qe}(k)$ is the measured acceleration signal of the vehicle body, m/s², $v_{te}(k)$ represents the theoretical vehicle speed measured by the encoder, m/s, $a_{te}(k)$ is the acceleration signal measured at the drive wheel, m/s², and $v_{qg}(k)$ denotes the actual speed measured by the GPS, m/s.

The observation model is given by:

$$\boldsymbol{Z}_i(k)=\boldsymbol{H}\cdot\boldsymbol{X}_i(k)+\boldsymbol{y}_i(k) \qquad i=1,2 \quad (4)$$

where, $\boldsymbol{H}$=diag(1, 1, 0, 1, 1,0) is the observation matrix, and the measurement noise $\boldsymbol{y}_i(k)$ is zero-mean Gaussian white noise with a covariance matrix $\boldsymbol{R}_i$.

The update process of the parallel Kalman filter can be divided into the following steps:

$$\hat{\boldsymbol{X}}_i(k\,|\,k-1)=\boldsymbol{A}\cdot\hat{\boldsymbol{X}}_i(k-1\,|\,k-1) \quad (5)$$

$$\boldsymbol{P}_i(k\,|\,k-1)=\boldsymbol{A}\cdot\boldsymbol{P}_i(k-1\,|\,k-1)\boldsymbol{A}^T+\boldsymbol{Q}(k-1) \quad (6)$$

$$\boldsymbol{K}_i(k)=\boldsymbol{P}_i(k\,|\,k-1)\cdot\boldsymbol{H}^T\cdot\left[\boldsymbol{H}\cdot\boldsymbol{P}_i(k\,|\,k-1)\cdot\boldsymbol{H}^T+\boldsymbol{R}_i(k+1)\right]^{-1} \quad (7)$$

$$\boldsymbol{P}_i(k\,|\,k)=\left[\boldsymbol{I}-\boldsymbol{K}_i(k)\cdot\boldsymbol{H}\right]\cdot\boldsymbol{P}_i(k\,|\,k-1) \quad (8)$$

$$\hat{\boldsymbol{X}}_i(k\,|\,k)=\hat{\boldsymbol{X}}_i(k\,|\,k-1)+\boldsymbol{K}_i(k)\cdot\left[\boldsymbol{Z}_i(k)-\boldsymbol{H}\cdot\hat{\boldsymbol{X}}_i(k\,|\,k-1)\right] \quad (9)$$

The state estimates from the two filters are fused through weighted averaging to obtain the global estimated state $\hat{\boldsymbol{X}}_g(k\,|\,k)$:

$$\hat{\boldsymbol{X}}_g(k\,|\,k)=\boldsymbol{W}_1\cdot\boldsymbol{X}_1(k\,|\,k)+\boldsymbol{W}_2\cdot\boldsymbol{X}_2(k\,|\,k) \quad (10)$$

where, $\hat{\boldsymbol{X}}_i(k|k\text{-}1)$ denotes the predicted state at time step k based on information available up to time *k-1,* while $\hat{\boldsymbol{X}}_i(k|k)$ represents the updated estimate at time step k after incorporating the measurement at time k. $\boldsymbol{P}_i(k|k\text{-}1)$ is the a priori estimation error covariance matrix, and $\boldsymbol{P}_i(k|k)$ is the a posteriori estimation error covariance matrix. $\boldsymbol{K}_i(k)$ represents the Kalman gain matrix. $\boldsymbol{W}_1$ and $\boldsymbol{W}_2$ represent the weighting matrices assigned to the two local Kalman filters during the state fusion process. These weights are determined based on the inverse of the corresponding a posteriori error covariance matrices. The weighting expression is defined as: $\boldsymbol{W}_i=(\boldsymbol{P}_1^{-1}+\boldsymbol{P}_2^{-1})^{-1}\cdot\boldsymbol{P}_i^{-1}, i=1,2$.

IMA-PKF Algorithm

Real-time tractor slip ratio estimation often relies on the fusion of multi-source sensor data, where the characteristics of measurement and process noise tend to be nonlinear and time-varying. These noise sources critically affect the accuracy of Kalman filter estimation. Conventionally, the selection of noise covariance

matrices $\boldsymbol{Q}$ and $\boldsymbol{R}$ depends on empirical tuning, trial-and-error methods, or offline experiments. However, such approaches assume prior statistical knowledge of the noise characteristics, which may not be valid in dynamic field conditions. Inappropriate choices of $\boldsymbol{Q}$ and $\boldsymbol{R}$ can lead to sluggish filter responses or even divergence of the estimation. To enhance adaptivity and robustness, this study introduces a mayfly algorithm-based approach to dynamically optimize the noise covariance matrices in the Kalman filter. The algorithmic framework of the proposed IMA-optimized PKF is illustrated in Fig. 1.

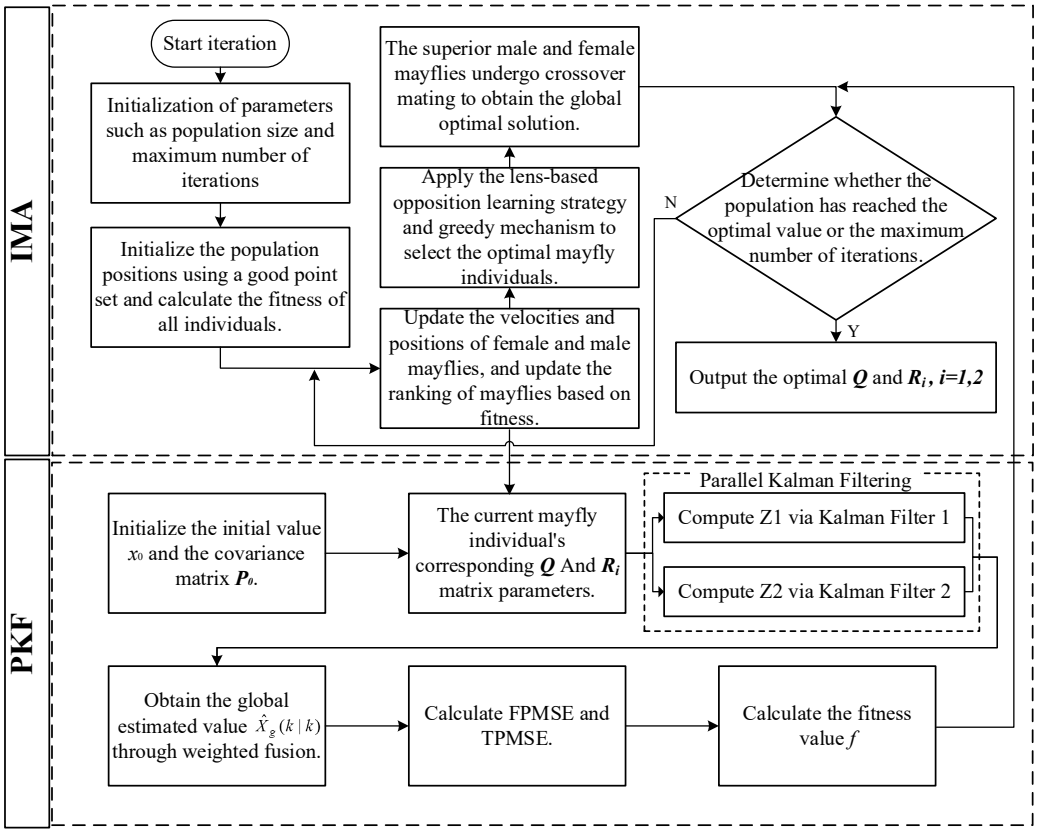

Fig.1 - IMA-PKF Algorithm Flowchart

Improved Mayfly Algorithm

The Mayfly Algorithm (MA) is a swarm intelligence optimization method inspired by the social behavior of mayflies (*Lizarraga et al., 2025; Zervoudakis & Tsafarakis, 2020*). It features good population diversity and strong local search ability, with high extensibility for domain-specific adaptations. However, MA often suffers from weak global exploration in early stages and reduced solution accuracy and stability in later stages, leading to premature convergence or entrapment in local optima. To overcome these drawbacks, this study introduces improvements in population initialization and the search mechanism.

(1) Good Point Set Initialization Strategy

The initial position of each mayfly individual refers to a point in a *D*-dimensional search space and is expressed as a vector of real-valued decision variables. Specifically, the position of the *i*-th individual is defined as $x_i^k = [x_i^1, x_i^2, ..., x_i^D]$, where $x_i{}^k$ denotes the value of the k-th coordinate (k = 1, 2, ..., D) of the i-th mayfly individual (i = 1, 2, ..., N), D is the problem dimension, and N is the population size. Each coordinate is a dimensionless variable representing a component of the optimization solution.

The initial positions are generated using the following formula:

$$x_i^k = a_k + rand\left(b_k - a_k\right) \quad (11)$$

where a_k and b_k are the lower and upper bounds of the k-th dimension, and $rand()$ is a uniform random number generator that produces values in the interval [0, 1].

Although the initial positions are generated using uniform random sampling within the defined bounds of the search space, the resulting distribution of individuals may still be uneven. As illustrated in Fig. 2(a), such randomness can lead to poor space utilization and a higher likelihood of premature convergence to local optima. To overcome this limitation, a good point set initialization strategy is introduced to improve the uniformity of the population distribution. The improved initialization method is defined as follows:

$$x_i^k = a_k + \{P_n(k)\}(b_k - a_k) \quad (12)$$

where $P_n(k)$ represents the good point set.

As illustrated in Fig. 2(b), the initialization method based on the good point set effectively avoids the randomness and local clustering inherent in traditional random initialization, thereby enhancing the global search capability of the MA.

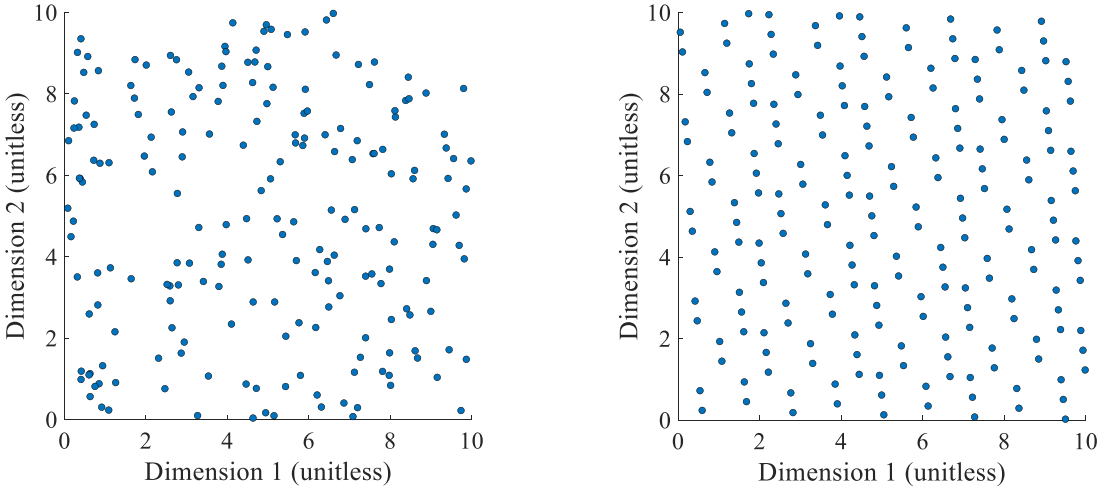

Fig. 2 - Initialization of mayfly

(a)Random Initialization；(b)Good Point Set Initialization

(2) Lens Imaging-Based Opposition Learning Strategy

To mitigate premature convergence and local optima entrapment in the mayfly population, this study introduces a lens imaging-based opposition learning strategy (*Yu et al., 2024*). aimed at enhancing population diversity and expanding exploration of the solution space.

This strategy is inspired by the optical imaging principle of a convex lens. Considering a bounded search interval [lb, ub], there exists an individual P with a height of *h,* whose projection on the X-axis is denoted by X (which represents the current global optimal solution). Let the reference point *O* be the midpoint of the interval, and a convex lens with focal length F is placed at O. According to the principle of convex lens imaging, the individual P is projected through the lens to form an inverted image P*, with height h* and a projection on the X-axis denoted as X*. Based on convex lens imaging theory, the following relationship can be established:

$$\frac{(ub+lb)/2 - X}{X^* - (ub+lb)/2} = \eta \quad (13)$$

where, η is the scaling factor, $\eta = h/h^*$.

The opposition point can be computed as:

$$X^* = \frac{ub+lb}{2} + \frac{ub+lb}{2\cdot\eta} - \frac{X}{\eta} \quad (14)$$

By adjusting the scaling factor *η*, the opposition solution can be dynamically varied, thereby enhancing the algorithm's local exploitation capability. In conventional lens imaging-based opposition learning strategies, *η* is constant, which limits the ability to effectively expand the population's search range. To address this limitation, this study introduces a Logistic chaos-based dynamic scaling strategy, in which the adaptive chaotic scaling factor is calculated as:

$$\eta = \eta_{\min} + (\eta_{\max} - \eta_{\min}) \cdot x_t \quad (15)$$

where x_t is a dynamic value generated by the Logistic chaotic map, updated as: $x_{t+1}=r\cdot x_t\cdot(1- x_t)$, The index t denotes discrete time steps and takes integer values t = 0,1,2,…, N, where N is the total number of iterations. *Here, r is the chaos control parameter, set to 4, and* $x_t \in (0,1)$.

A greedy selection mechanism is further introduced to evaluate and retain improved individuals generated through the opposition learning process. The mathematical model of the greedy selection is expressed as:

$$X_{new}(t)=\begin{cases}X^*,\ f(X)\geq f(X^*)\\ X\ ,\ f(X)<f(X^*)\end{cases} \quad (16)$$

where $f(\ )$ denotes the fitness function that quantifies the quality or objective value of an individual solution and evaluates the performance level of each candidate solution X under the optimization objective.

Noise Adaptation Based on the Improved Mayfly Algorithm

In the Parallel Kalman Filter (PKF), the process noise covariance matrix $\boldsymbol{Q}$ and the measurement noise covariance matrix $\boldsymbol{R}$ are critical parameters that directly affect the accuracy and stability of state estimation. However, in practical applications, conventional Kalman filtering often suffers from inaccurate modeling and unknown or time-varying noise statistics, making it difficult to determine appropriate values for these matrices. Traditional Kalman filters typically assume that $\boldsymbol{Q}$ and $\boldsymbol{R}$ are constant, but such an assumption often fails to meet the requirements of real-world scenarios. Inappropriate settings may result in sluggish filter response, increased estimation bias, or even filter divergence. To ensure unbiased estimation and filter stability, it is essential to select appropriate values for the process and measurement noise covariance matrices. Therefore, a dynamic adjustment mechanism based on the Improved Mayfly Algorithm (IMA) is introduced to optimize $\boldsymbol{Q}$ and $\boldsymbol{R}$ in real time, thereby enhancing the adaptive capability of the Kalman filter.

Let $\boldsymbol{Q}_u$ and $\boldsymbol{R}_u$ denote the process noise covariance and measurement noise covariance matrices actually used by the Kalman filter, respectively:

$$\begin{cases}\boldsymbol{Q}_u=\boldsymbol{Q}+\Delta\boldsymbol{Q}\\ \boldsymbol{R}_u=\boldsymbol{R}+\Delta\boldsymbol{R}\end{cases} \quad (17)$$

where $\boldsymbol{Q}$ and $\boldsymbol{R}$ are the true process and measurement noise covariance matrices, and $\Delta\boldsymbol{Q}$ and $\Delta\boldsymbol{R}$ represent the deviations of the applied matrices from the true values.

The True Mean Squared Error (TMSE) and the Filter Calculated Mean Squared Error (FMSE) are typically introduced as evaluation metrics When TMSE closely matches FMSE, the estimated covariances $\boldsymbol{Q}_u$ and $\boldsymbol{R}_u$ are more consistent with the true noise characteristics $\boldsymbol{Q}$ and $\boldsymbol{R}$. However, due to the fact that the noise covariance is generally unknown or there is model bias, it is quite difficult to directly calculate the TMSE and FMSE. So, the Filter Calculated Prediction Mean Squared Error (FPMSE) and the True Prediction Mean Squared Error (TPMSE) are introduced as alternative indicators to estimate the system errors online, providing a practical basis for evaluating filter performance under unknown noise conditions (Ge et al., 2023; Ge et al., 2016). The TPMSE is calculated as follows:

$$\boldsymbol{p}_{zk}^{m}=\boldsymbol{H}_k\left(\boldsymbol{A}\boldsymbol{P}_{k-1|k-1}^{m}\boldsymbol{A}^T+\boldsymbol{Q}_{k,k-1}\right)\boldsymbol{H}_k^T+\boldsymbol{R}_k\approx\frac{1}{k}\sum_{i=1}^{k}\boldsymbol{e}_i\boldsymbol{e}_i^T \quad (18)$$

where $\boldsymbol{e}_k$ denotes the innovation at time step k, $\boldsymbol{e}_k=\boldsymbol{Z}(k)-\boldsymbol{H}\cdot\hat{\boldsymbol{X}}\left(k\,|\,k-1\right)$.

The FPMSE is calculated as follows:

$$\boldsymbol{P}_{zk}^{f}=\boldsymbol{H}_k P_{k|k-1}^{f}\boldsymbol{H}^T+\boldsymbol{R}_k^u \quad (19)$$

To ensure optimal filter performance, the fitness function of the improved mayfly algorithm is defined as the minimum 2-norm of the difference between FPMSE and TPMSE:

$$f\left(k\right)=\min\left(\|\,\boldsymbol{P}_{zk}^{f}-\boldsymbol{P}_{zk}^{m}\,\|_2\right) \quad (20)$$

Online measurement system of tractor slip ratio

In order to verify the effectiveness and feasibility of the proposed algorithm, an online measurement system was established, which was installed on the tractor ploughing unit as shown in Fig.3.

The system primarily consists of photoelectric encoders, a combined inertial navigation mobile station (including GNSS and IMU), a laser ranging sensor, an inclination sensor, a USB-6210 data acquisition card, and an upper computer. The actual vehicle speed was estimated by fusing the front wheel speed measured by the encoder with the GNSS speed. The theoretical vehicle speed was derived from the rear wheel speed captured by the encoder, reflecting the motion of the driven wheel. The upper computer was used to deploy the algorithm proposed in this paper, and the platform was later used for field experiments to verify its effectiveness under real-world working conditions. The system integrates multi-sensor fusion technology and real-time computing capabilities, providing a solid foundation for the deployment of the proposed algorithm and the evaluation of its measurement performance under complex plowing conditions.

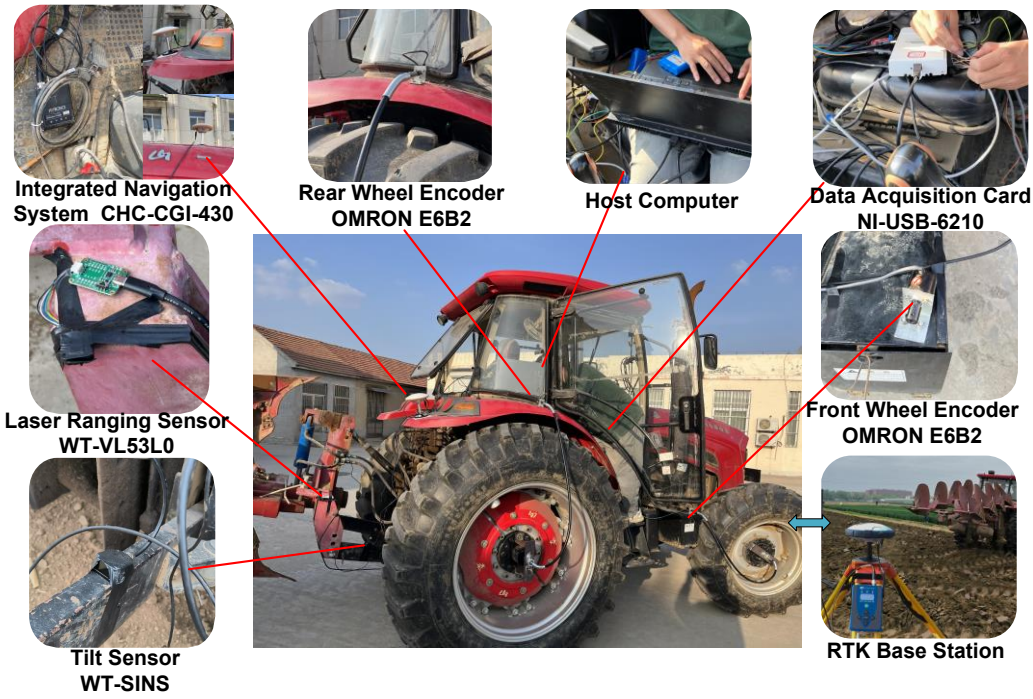

Fig. 3 - Tractor Slip Ratio Acquisition System

RESULTS AND DISCUSSIONS

Simulation Analysis

To verify the effectiveness of the proposed algorithm, simulated measurement signals were generated in MATLAB based on typical plowing operation conditions. The tractor working speed was assumed to vary within the range of 1 to 3 m/s, which covers the majority of practical plowing speeds. A portion of the simulated signals is shown in Fig. 4. All signals were corrupted with zero-mean Gaussian white noise with a standard deviation equal to 5% of the signal amplitude. The measurement noise covariance matrices were defined as: $\boldsymbol{R}_1$=diag(0.1^2, 0.06^2, 0, 0.11^2, 0.06^2, 0), $\boldsymbol{R}_2$=diag(0.13^2, 0.06^2, 0, 0.11^2, 0.06^2, 0). The simulation time was 30 s with a sampling frequency of 50 Hz. KF, Particle Swarm Optimization-based Parallel Kalman Filter (PSO-PKF), MA-PKF, and the IMA-PKF were selected to estimate the slip ratio. The simulation comparison results are shown in Fig. 5.

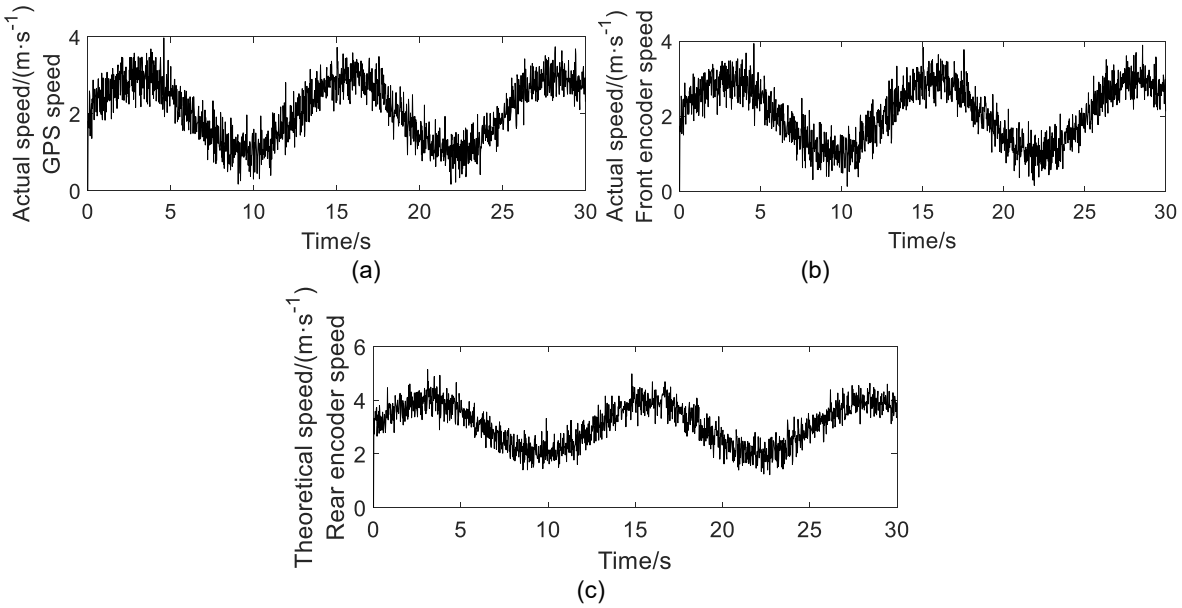

Fig. 4 - Simulated Sensor Measurement Signals s

(a) GPS speed; (b) Front encoder speed; (c) Rear encoder speed

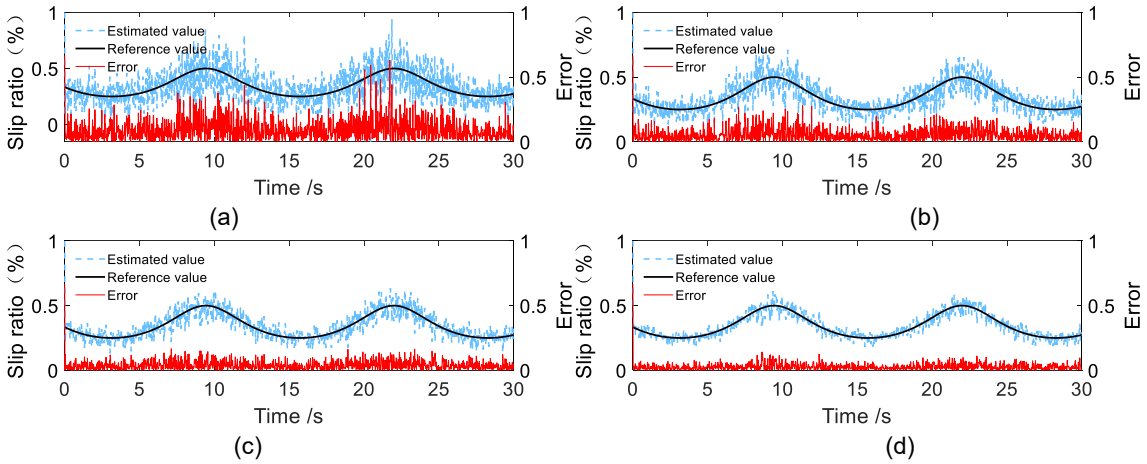

Fig. 5 - Comparison of Slip Ratio Signals from Different Algorithms

(a)KF; (b)PSO-PKF; (c)MA-PKF; (d)IMA-PKF

As shown in Fig. 5, there are significant differences in slip ratio estimation accuracy among 4 algorithms. The mean absolute errors (MAE) of KF, PSO-PKF, MA-PKF, and IMA-PKF are 0.0714, 0.0433, 0.0348, and 0.0202, respectively, while the corresponding root mean squared errors (RMSE) are 0.0848, 0.0567, 0.0423, and 0.0214. Compared with the original KF algorithm, both MAE and RMSE are reduced in PSO-PKF, MA-PKF, and IMA-PKF. Specifically, the MAE of MA-PKF and PSO-PKF is reduced by 39.3% and 51.3%, respectively, and the RMSE is reduced by 33.1% and 50.1%. The IMA-PKF algorithm achieves the best performance, with MAE and RMSE reduced by 71.7% and 74.8%, respectively, relative to KF, demonstrating the most effective error suppression. From the results, although the slip ratio estimated by the KF algorithm generally follows the trend of the reference signal, it exhibits noticeable fluctuations at certain time. In contrast, the estimates from the MA-PKF and PSO-PKF algorithms are smoother and more stable, with reduced errors and more uniform error distribution. The IMA-PKF algorithm yields the most accurate estimation results, effectively suppressing noise and providing higher measurement precision.

To further assess the anti-interference robustness of the IMA-PKF under diverse and realistic perturbation scenarios, a Monte Carlo simulation comprising 100 independent trials was conducted. In each trial, 5 transient disturbances were superimposed onto the actual vehicle speed signal to emulate unpredictable field conditions. These disturbances were constructed using half-sine waveforms with randomly sampled parameters. Specifically, injection times were drawn from Gaussian distributions centered at 6 s, 10 s, 15 s, 20 s, and 25 s, while amplitudes and frequencies were sampled from uniform distributions within ±0.4-0.8 m/s and 4.5-5.5 Hz, respectively. Each disturbance lasted for 0.2 s. This randomized design was intended to mimic non-stationary and transient noise sources such as terrain shocks or sporadic sensor anomalies. All four algorithms were tested under these conditions to evaluate their estimation consistency and robustness.

A representative example of the disturbed GPS-measured vehicle speed signal is shown in Fig. 6, while Fig. 7 compares the resulting slip ratio estimation errors under the 100 Monte Carlo trials.

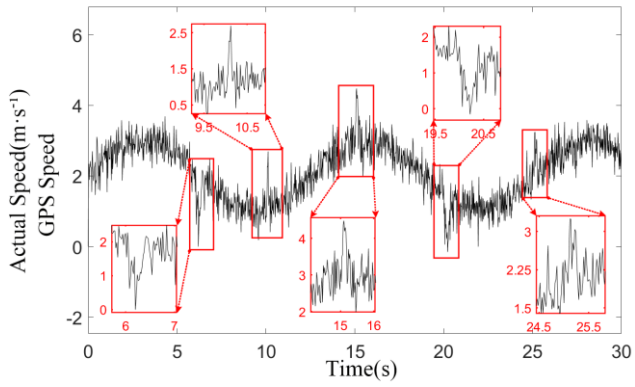

Fig. 6 - GPS Vehicle Speed with Disturbances

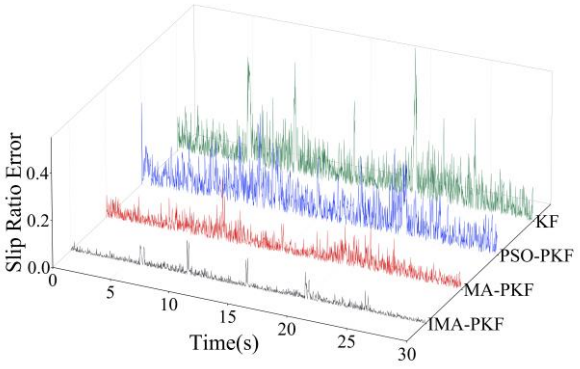

Fig. 7 - Comparison of Absolute Slip Ratio Errors

The mean absolute error (MAE) values for KF, PSO-PKF, MA-PKF, and IMA-PKF were 0.0723, 0.0721, 0.0438, and 0.0282, respectively; the corresponding RMSE values were 0.0795, 0.0865, 0.0589, and 0.0359; and the maximum absolute errors reached 0.6262, 0.3977, 0.2701, and 0.1464, respectively. These results indicate that while PSO-PKF improved robustness over the conventional KF, it remained sensitive to severe disturbances. MA-PKF exhibited better stability and denoising capacity, but IMA-PKF consistently delivered the most accurate and reliable performance across all trials, demonstrating superior resistance to transient interference and enhanced estimation robustness.

Field Experiment Results and Discussion

To validate the performance and reliability of the proposed algorithm, field experiments were carried out under actual plowing conditions at the Technology Demonstration Base of Shandong Agricultural University. The experimental setup included the Taishan-1404A tractor and 1LF-435 reversible plough, and the main parameters are summarized in Table 1. During the experiment, RTK-GNSS was employed as the reference measurement device to validate the effectiveness of the proposed algorithm in estimating the tractor slip ratio. The laser ranging sensor and inclination sensor were used to monitor the tillage depth. To ensure consistent operation and realistic evaluation across varying working depths, the throttle opening was kept constant during each test, and the resulting average plowing speeds were approximately 6.48 km/h (15 cm), 5.83 km/h (20 cm), 5.44 km/h (25 cm), and 5.04 km/h (30 cm), respectively.

Table 1

Main Parameters of the Experimental Tractor and Plough

Equipment Name	Parameter	Value
Taishan-1404A tractor	Overall Dimensions (L×W×H) [mm]	5000×2510×3115
	Wheelbase [mm]	2550
	Rated Power [kW]	103
	Maximum Drawbar Pull [kN]	28
	Minimum Operating Weight [kg]	5260
1LF-435 reversible plough	Overall Dimensions (L×W×H) [mm]	4000×1600×1850
	Total Weight [kg]	1470
	Number of Plough Bodies	4×2
	Working Width per Share [mm]	350
	Maximum Working Depth [cm]	35

The experimental field measured 200 m in length and 300 m in width. The length of each ploughing operation in the experiment was approximately 200 m. Since the field had been previously plowed, compaction treatment was applied to meet the experimental requirements. To investigate the algorithm's performance under varying tillage depths, the field was divided into four subplots, each assigned a specific working depth: 15 cm, 20 cm, 25 cm, and 30 cm. During the experiments, the tractor was driven in a straight line with the differential lock engaged. Once the reversible plow reached the target depth, the throttle opening was maintained at a constant level. The field tests were conducted under ambient temperatures ranging from 12 °C to 18 °C, with weather conditions transitioning from light rain to overcast skies. As shown in Fig. 8, all field experiments were carried out under realistic tillage conditions in the prepared test area.

The advantages of IMA-PKF over PSO-PKF and MA-PKF have been verified through simulation experiments. Due to the limitations of the plot size and the complexity of the algorithm calculation, only the IMA-PKF algorithm and the original KF algorithm were selected for comparison.

Fig.9 presents the comparison of tractor slip ratio estimation results under 4 plowing conditions using the IMA-PKF and KF algorithms. The measured values and reference values exhibit similar trends, indicating that the IMA-PKF algorithm can accurately track the dynamic changes in slip ratio. The algorithm provides estimates that closely match the actual values and demonstrates good stability. It is worth noting that the sudden increase in slip ratio observed in Fig. 9(c) during the later stage of the operation is likely caused by external disturbances, such as the plow encountering rocks during the tillage process. The mean absolute error (MAE) and root mean squared error (RMSE) of the slip ratio estimated by both the IMA-PKF and KF algorithms are shown in Fig. 10.

Fig. 8 - Field Test Site

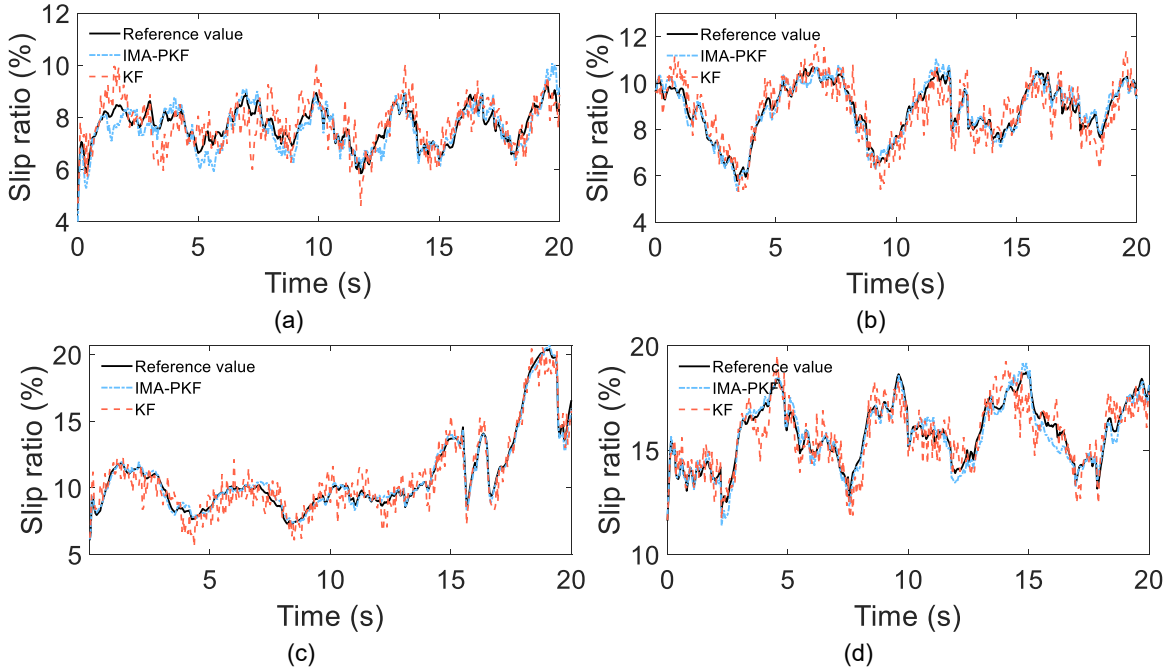

Fig. 9 - Experimental Slip Ratio Estimation Curves

(a) Tillage Depth: 15 cm; (b) Tillage Depth: 20cm; (c) Tillage Depth: 25cm; (d) Tillage Depth: 30cm

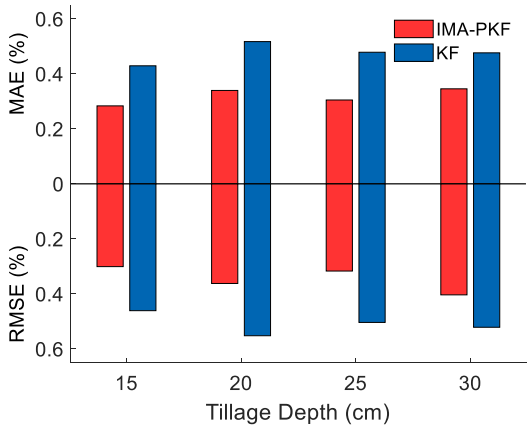

Fig. 10 - Statistical Results of Experimental Data

As shown in Fig. 10, under all four tillage depth conditions, the proposed IMA-PKF algorithm demonstrates significantly improved performance compared to the conventional KF algorithm. Specifically, the MAE of the IMA-PKF algorithm is reduced by 33.95%, 34.35%, 36.29%, and 27.47%, respectively, while the RMSE is reduced by 34.67%, 34.42%, 37.06%, and 22.60%, respectively. These experimental results confirm that the IMA-PKF algorithm exhibits superior measurement performance under complex operating conditions and can effectively improve the accuracy of tractor slip ratio estimation. While the proposed IMA-PKF algorithm exhibits strong performance under the tested conditions, further validation is needed to assess its general applicability across various soil types, equipment configurations, and operating scenarios, particularly in highly resistant or hard soils.

CONCLUSIONS

(1) A tractor slip ratio online measurement method was proposed in the paper. This method is based on the improved firefly algorithm optimized parallel Kalman filter (IMA-PKF). By integrating data from multiple sensors and adaptively estimating noise, this method can dynamically adapt to changes in noise and achieve online accurate measurement of tractor slip ratio under different plowing conditions.

(2) Simulation results show that under non-interference conditions, the IMA-PKF algorithm achieves a root mean squared error (RMSE) of 0.0214, which is 74.8% lower than that of the conventional KF algorithm, and it also outperforms PSO-PKF and MA-PKF in terms of estimation accuracy. In terms of anti-interference capability, the IMA-PKF algorithm maintains the lowest estimation error even after the introduction of disturbance points, with an RMSE of 0.0359, demonstrating superior stability and robustness.

(3) A set of online measurement system for tractor slip ratio was established. And field experiments have confirmed that the estimated slip ratio measured by IMA-PKF are highly consistent with the reference values, with the maximum error being only 1.94% and the deviation being less than 2%. Under different tillage depths, compared with KF, IMA-PKF reduces the average absolute error (MAE) and root mean square error (RMSE) by up to 36.29% and 37.06% respectively, demonstrating its reliability under complex conditions and providing support for the improvement of tractor performance.

In future work, the test scope will be expanded to include different soil conditions such as harder or more resilient soils, various humidity levels, as well as different tractor types and farm implements. This will help verify the reliability and adaptability of the IMA-PKF algorithm under complex operating conditions.

ACKNOWLEDGEMENT

This research was supported by the project ZR2022QE217 supported by Shandong Provincial Natural Science Foundation.

REFERENCES

[1] Bisht, S. S., & Singh, M. P. (2014). An adaptive unscented Kalman filter for tracking sudden stiffness changes. *Mechanical Systems Signal Processing*, *49*(1-2), 181-195.

[2] Boisvert, M., & Micheau, P. (2016). Estimators of wheel slip for electric vehicles using torque and encoder measurements. *Mechanical Systems and Signal Processing*, *76-77*, 665-676. https://doi.org/10.1016/j.ymssp.2016.02.017

[3] Cao, Q., Zhou, Z., Zhang, M., Xi, Z., & Xi, J. (2015). Algorithm and verification for estimating tractor driving wheel slip rate（拖拉机驱动轮滑转率估算法与验证）. *Transactions of the Chinese Society of Agricultural Engineering*, *31*(23), 35-41.

[4] De Bruijn, F., & Gill, E. (2014). Influence of sensor and actuator errors on impulsive satellite formation control methods. *Acta Astronautica*, *94*(2), 608-618. https://doi.org/10.1016/j.actaastro.2013.08.015

[5] Deng, Y., Zhao, Z., Yang, Y., & Yu, Q. (2024). Vision and Radars Fusion Algorithm Based on Distributed Robust Kalman Filters in ADAS（ADAS 系统视觉与毫米波雷达分布式抗差卡尔曼滤波融合算法). *Automotive Engineering*, *46*(05), 805-815. https://doi.org/10.19562/j.chinasae.qcgc.2024.05.007

[6] Du, X., Hong, F., Ma, Z., Li, Y., & Zhao, L. (2024). State-of-the-art and Prospect on Sliding Identification and Control of Agricultural Machinery（农业装备行驶滑动辨识与控制研究现状与展望） *Transactions of the Chinese Society for Agricultural Machinery*, *55*(08), 1-20.

[7] Ge, Q. B., Hu, X. M., Li, Y. Y., He, H. L., & Song, Z. H. (2023). A Novel Adaptive Kalman Filter Based on Credibility Measure. *Ieee-Caa Journal of Automatica Sinica*, *10*(1), 103-120. https://doi.org/10.1109/jas.2023.123012

[8] Ge, Q. B., Shao, T., Duan, Z. S., & Wen, C. L. (2016). Performance Analysis of the Kalman Filter With Mismatched Noise Covariances. *Ieee Transactions on Automatic Control*, *61*(12), 4014-4019. https://doi.org/10.1109/tac.2016.2535158

[9] Han, B., Zhu, S., Du, X., Liu, Y., Li, Z., & ZHU, Z. (2023). Estimation Method of Slip Ratio for Tractor Driving Wheels Based on Multi-sensor Fusion（基于多传感器融合的拖拉机驱动轮滑转率估算方法） *Transactions of the Chinese Society for Agricultural Machinery*, *54*(S1), 402-410+426.

[10] Hashemipour, H. R., Roy, S., & Laub, A. J. (1988). Decentralized structures for parallel Kalman filtering. *Transactions on automatic control*, *33*(1), 88-94.

[11] Li, D. Q., Yu, X. D., Liu, S. L., Dong, X., Zang, H. Z., & Xu, R. (2022). Wind power prediction based on PSO-Kalman [Article; Proceedings Paper]. *Energy Reports*, *8*, 958-968.

https://doi.org/10.1016/j.egyr.2022.02.077

[12] Li, S., Li, J., & Feng, G. (2024). Road roughness recognition based on GA-LSTM adaptive Kalman filtering（基于 GA-LSTM 自适应卡尔曼滤波的路面不平度识别）. *Journal of Vibration and Shock*, *43*(09), 121-130. https://doi.org/10.13465/j.cnki.jvs.2024.09.015

[13] Li, S., Yang, L., Qu, R., Sun, P., & Yu, D. (2024). Slip rate control method based on model predictive control（基于模型预测控制的滑移率控制方法）. *Journal of Jilin University (Engineering and Technology Edition)*, *54*(09), 2687-2696. https://doi.org/10.13229/j.cnki.jdxbgxb.20221401

[14] Liu, C. W., Li, H. J., & Wang, Z. H. (2024). FastTrack: A Highly Efficient and Generic GPU-Based Multi-object Tracking Method with Parallel Kalman Filter. *International Journal of Computer Vision*, *132*(5), 1463-1483. https://doi.org/10.1007/s11263-023-01933-4

[15] Lizarraga, E., Valdez, F., Melin, P., & Castillo, O. (2025). A Hybrid Enhanced Mayfly Optimization Algorithm with Improved Performance through Fuzzy-Based Automatic Parameter Adaptation. *Computación y Sistemas*, *29*(2), 615-631. https://doi.org/10.13053/CyS-29-2-5709

[16] Peng, L., Shijun, S., Wei, L., Yuqian, Z., & Weichen, Y. (2025). DESIGN AND EXPERIMENT OF GRAIN HARVESTER YIELD MONITORING SYSTEM BASED ON MULTI-SENSOR FUSION. *INMATEH-Agricultural Engineering*, *75*(1), 763-776. https://doi.org/https://doi.org/10.35633/inmateh-75-65

[17] Pranav, P. K., Tewari, V. K., Pandey, K. P., & Jha, K. R. (2012). Automatic wheel slip control system in field operations for 2WD tractors. *Computers and Electronics in Agriculture*, *84*, 1-6. https://doi.org/10.1016/j.compag.2012.02.002

[18] Raheman, H., & Jha, S. (2007). Wheel slip measurement in 2WD tractor. *Journal of terramechanics*, *44*(1), 89-94.

[19] Sun, B., Zhang, Z., Qiao, D., Mu, X., & Hu, X. (2022). An improved innovation adaptive Kalman filter for integrated INS/GPS navigation. *Sustainability*, *14*(18), 11230.

[20] Suzuki, H. (2013). Dynamic state estimation in vehicle platoon system by applying particle filter and unscented kalman filter. *Procedia Computer Science*, *24*, 30-41.

[21] Wang, W., He, N., Yao, K., & Tong, J. (2021). Improved Kalman filter and its application in initial alignment. *Optik*, *226*, 165747.

[22] Wen, T., Liu, J. Z., Cao, Y., & Roberts, C. (2023). Parallel Kalman filter group integrated particle filter method for the train nonlinear operational status high-precision estimation under non-Gaussian environment. *Accident Analysis and Prevention*, *190*, 107158. https://doi.org/10.1016/j.aap.2023.107158

[23] Xia, G., Xia, Y., Tang, X., Gao, J., Wang, S., & Sun, B. (2021). Speed regulation control of the dual-flow transmission system for a tractorusing slip rate-resistance interval division（采用滑转率-阻力区间划分法的拖拉机双流传动系统调速控制）. *Transactions of the Chinese Society of Agricultural Engineering*, *37*(03), 47-55.

[24] Xiong, L., Xia, X., Lu, Y. S., Liu, W., Gao, L. T., Song, S. H., & Yu, Z. P. (2020). IMU-Based Automated Vehicle Body Sideslip Angle and Attitude Estimation Aided by GNSS Using Parallel Adaptive Kalman Filters. *Ieee Transactions on Vehicular Technology*, *69*(10), 10668-10680. https://doi.org/10.1109/tvt.2020.2983738

[25] Yu, F., Guan, J., Wu, H., Chen, Y., & Xia, X. (2024). Lens imaging opposition-based learning for differential evolution with cauchy perturbation. *Applied Soft Computing*, *152*, 111211.

[26] Zervoudakis, K., & Tsafarakis, S. (2020). A mayfly optimization algorithm. *Computers & Industrial Engineering*, *145*, 106559. https://doi.org/10.1016/j.cie.2020.106559

[27] Zhang, Shuo, Luo, Yanqing, Jia, Lei., Wen, JingMing, Jin, HongLing, Chen, Y. (2025). Hardware-in-the-loop simulation for drive wheel slip control of high-power tractor for ploughing operation. *INMATEH-Agricultural Engineering*, *75*(1), 390-402. https://doi.org/https://doi.org/10.35633/inmateh-75-33